International Journal of Hydrogen Energy 93 (2024) 937–947

Contents lists available at ScienceDirect

International Journal of Hydrogen Energy

journal homepage: www.elsevier.com/locate/he

Two-phase flow effect on methane conversion in pyrolysis reactors embedding molten salts or metals

Valentina Biagioni [a], Giuseppe Procopio [a], Antonio Brasiello [a], Luca Turchetti [b], Stefano Cerbelli [a], Maria Anna Murmura [a,*]

[a] DICMA Sapienza Università di Roma (Italy), Via Eudossiana 18, 00184 Rome, Italy
[b] ENEA - Italian National Agency for New Technologies, Energy and Sustainable Economic Development, Italy

ARTICLE INFO

Keywords:
Methane cracking
Molten media
Multiscale approach
Residence time
Bubble diameter
Effective velocity

ABSTRACT

In this work, we numerically investigate the impact of flowrate, sparger and reactor geometry on methane conversion in lab-scale cylindrical pyrolysis reactors embedding molten salts or metals. A multiscale approach is enforced, where a diffusion-reaction model yielding the conversion vs time within a single rising bubble is combined with the average residence time of gas bubbles obtained through the two-phase turbulent bubbly flow model. We find that the relative size of the sparger and the height-to-diameter ratio of the molten medium are key parameters for controlling the average residence time of the bubbles, which always results lower than that predicted by the terminal velocity of a single bubble rising in an overall static melt. The highest relative discrepancy (order 300%) between the single-bubble estimate and the CFD-based residence time is found in the case of molten salts in low-aspect ratio reactors fed by small spargers. The physical mechanism underpinning the influence of geometric parameters on the overall conversion is addressed in detail, together with the impact of two-phase flow effects on the estimation of bubble size in laboratory scale bubble reactors.

1. Introduction

Hydrocarbon pyrolysis offers the most direct route to CO_2-free hydrogen production, yielding what is today termed "turquoise hydrogen". However, hydrocarbon pyrolysis can potentially be used to produce green hydrogen, if the process is fed with renewable feedstocks and energy sources, e.g., biomethane and heat from concentrating solar thermal plants [1–5].

For the simplest hydrocarbon, namely methane, the pyrolysis reaction

$$CH_{4\,(g)} \rightleftharpoons C_{(s)} + 2H_{2\,(g)} \qquad \left(\Delta H_{298} = 74.9\ \mathrm{kJ/mol}\right) \tag{1}$$

is moderately endothermic and determines an overall increment in the number of moles in the gas phase. From a thermodynamic standpoint methane pyrolysis is therefore favored at high temperatures and low pressures. Appreciable values of the equilibrium conversion (of order few percentage points) can be predicted at atmospheric pressure at temperatures above 300 °C. At 1000 °C, the equilibrium conversion is above 85% at 10 atm, and above 90% for pressure values below 5 atm [6]. Nevertheless, kinetic issues do not allow to obtain near-equilibrium conversions below 1100–1200 °C at appreciable rates, unless transition or noble metals (Ni, Fe, Cu, Co, Pd, Pt to name but few examples) are used as catalysts [7–10]. A massive effort in the search for solid catalysts for hydrocarbon pyrolysis has been put forward in the last decades in order to single out the best combination of porous ceramic support and embedded metal providing highest and durable activity in assigned temperature ranges [11]. Notwithstanding some encouraging results, a major shortcoming against the use of solid catalysts in cracking reactions is their rapid deactivation due to significant deposition of the solid carbon product, which makes the continuous implementation of the hydrogen production process impractical [12–15]. For this reason, alternative scenarios for the reaction environment have been scrutinized. Hinging on the observation that the auto-catalytic activity of the solid carbon product depends sensitively on the hydrocarbon undergoing cracking, a strategy to extend the catalyst activity has been co-feeding methane and/or natural gas with aromatics and unsaturated hydrocarbons (e.g. benzene, ethylene, acetylene), which naturally yield a solid carbon product with high catalytic activity [16]. Yet, the high cost of the co-feeding makes the process economically unattractive. An altogether different approach was first devised in a pioneering US patent nearly a century ago by Tyrer [17], who first proposed to carry out the pyrolysis reaction in molten iron. To use his own words, the molten medium "has the property of dissolving and thus 'fixing' the carbon". Because most molten metal are characterized by a density significantly higher than that of

* Corresponding author.
E-mail address: mariaanna.murmura@uniroma1.it (M.A. Murmura).

https://doi.org/10.1016/j.ijhydene.2024.10.362
Received 7 August 2024; Received in revised form 30 September 2024; Accepted 25 October 2024
Available online 6 November 2024

solid carbon, the latter floats at the liquid–gas interface at the top of the bath, making it possible to use mechanical separation methods to skim the solid product [18–20]. One more advantage of using molten metals is related to their high thermal conductivity, which ensures a homogeneously distributed temperature field for the reaction and efficient heat transport from the bulk liquid to the gas–liquid interface. Molten salts have also been considered and tested as a liquid bath for pyrolysis in view of their negligible vapor pressure at the high operating temperatures of the process. Compared to molten metals, molten salts are easier to separate from the solid product collected in the reactor although their density difference with solid carbon is much lower. In any case, even in molten salts, the separation of the solid carbon can be achieved by flotation, thus avoiding the deposition of carbon particles onto the reactor walls. [21–23]. Notwithstanding the intense research effort put forward in the past three decades for characterizing pyrolysis in molten media, most of the key issues about the process are far from being fully understood. These issues can be grouped into three separate if interacting processes as follows:

- Bubble formation and release at the sparger. The crucial information here is the size distribution of the released bubbles. Owing to possible break-up and coalescence of neighboring newborn bubbles while they are being formed, the type of the sparger (i.e. whether a disordered microporous material or an ordered array of microcapillaries) plays a crucial role. Specifically, because the average distance of micropores of disordered materials can hardly be controlled in the manufacturing process of microporous spargers, significant coalescence of the bubbles before detachment can be expected for this type of sparger [24–26]. This makes the final size of the bubbles at detachment very weakly correlated with the average pore size of the material. When combined with the difficulty of a direct experimental determination of the bubble size by optical methods (due to the lack of optical transparency of the melt), this uncertainty forces to consider the size distribution of the bubbles entering the reaction environment essentially as an unknown variable to be correlated with integral measures characterizing the process, such as overall gas hold-up and conversion.

- Two-phase reacting flow. Owing to the increasing number of moles in the gas phase caused by the pyrolysis reaction, a full coupling between reaction within the single bubbles and two-phase flow due to the collective momentum transfer of the rising bubbles to the liquid should be considered. Also, the possible break-up and coalescence of bubbles within the reaction bath would require to solve a population balance model coupled with the two-phase flow [27].
- Heat transport. Notwithstanding the high thermal conductivity of molten metals [28], some temperature gradients within the melt could be expected, especially at the industrial scale implementation of the process. Clearly, energy transport is yet one more equation that must be solved simultaneously with the two-phase reacting flow model.

From all of these observations, it follows that the accurate modeling of all the physico-chemical processes taking place in the molten medium is a formidable task, unapprochable at any practical rate in view of the fact that most of the thermodynamic, transport and kinetic parameters entering the local balance equations are neither directly accessible to experimental determination nor accurately predicted by theoretical models. The situation is further complicated by the fact that the flow regimes may change significantly depending on the gas hold up within the reactor, which in turn depends on the geometric characteristics of the reactor and sparger and the gas flow rate. For this reason, giving up on the idea of constructing a fully predictive theoretical model, we rather seek for some computationally affordable approach capable of grasping the essential interplay between transport and kinetics in the homogeneous flow regime, therefore allowing to correlate the different variables involved in the process on some firm if simplified physical grounds. To this end, we use a multiscale approach, obtained by combining the description of species transport and reaction within a single bubble with the macroscopic two-phase fluid dynamics that takes into account the velocity patterns of the liquid set in motion by the rising gas. As regards the small scale, the conversion vs. time of the single bubble is described by an analytical model recently proposed by some of these authors [29,30] . This model was validated against the solution of the complete set of momentum, energy and species local balance equations enforced on a moving boundary domain to account for the bubble expansion due to the reaction advancement, and was proven to provide a consistent interpretation of experimental data of methane pyrolysis in Ni-Bi melts [7]. The conversion-vs.-time model of the single bubble is then combined with information on the average residence time of the gas bubbles estimated through the solution of a two-phase turbulent bubbly flow model. In this model, the relative velocity of the gas with respect to the liquid depends on bubble size, consistently with the expression assumed for the drag coefficient. In a static medium (i.e. for a single bubble rising in an infinitely extended quiescent fluid), this velocity is equal to the terminal rising velocity of the bubble, whereas for higher gas flow rates the collective buoyancy action of the bubbles sets the liquid phase in a recirculating motion. We show how, depending on the spatial distribution of the gas, due to liquid recirculation, the absolute gas velocity in the reactor departs from the terminal rising velocity of the single bubble. As a consequence, the average residence time of the gas phase and methane conversion deviate from those estimated from the terminal rising velocity of the single bubble for any given height of the melt.

The article is organized as follows. Section 2 introduces the multiscale approach, starting with the concise description of the analytical model for the conversion within the single bubble and a detailed description of the bubbly flow approach. Section 3 reports the results for the two-phase flow in different reactor geometries and operating conditions and its consequences on the overall conversion of the pyrolysis reaction. Concluding remarks and possible directions of future work are discussed in Section 4.

2. Materials and methods

The approach followed here consists in combining a 0D model, in which methane conversion is related only to time, and which was developed in previous studies [29], with a 2D analysis of turbulent gas–liquid flow. The aim has been to obtain a realistic prediction of methane conversion in lab scale reactors, achieved by removing the commonly employed assumption of gas bubbles rising at their slip velocity, while maintaining a low computational cost because the kinetic model is essentially superimposed on the flow model rather than solved simultaneously. The details of this procedure are reported in the following paragraphs.

2.1. System geometry

The scheme of the system geometry is depicted in Fig. 1, together with the relevant parameters and the reference frame. Cylindrical symmetry about the z-axis is assumed throughout. By fixing the reactor diameter, D_m, as reference length (where the subscript "m" stands for "melt"), the system geometry is uniquely specified by the sparger-to-reactor diameter, $d_s = D_s/D_m$, and the aspect ratio $h = H/D_m$. Methane is assumed to be fed through a sparger placed in the middle of the reactor, at $z = 0$, forming bubbles that rise through the melt whilst reacting to form hydrogen and carbon. The gaseous product is collected from the top of the reactor, along with unreacted methane. Solid carbon is assumed to float on the top of the liquid melt.

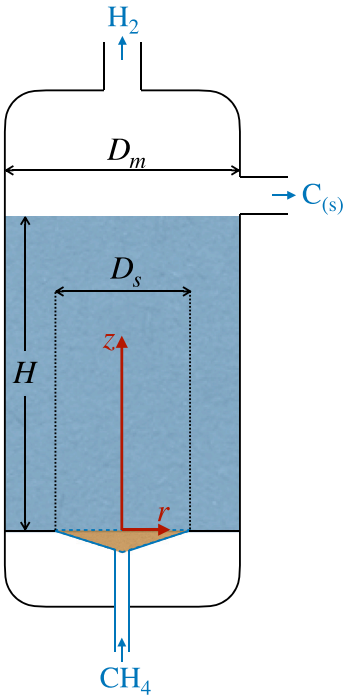

Fig. 1. Geometry and relevant parameters of the system investigated.

2.2. CFD analysis of the turbulent gas–liquid flow

The bubbly flow model provides a relatively simple means to approach two-phase gas–liquid flows, both in laminar and turbulent regime, able to capture most of the relevant physics in a wide variety of settings [31]. Preliminary tests (not discussed for brevity) showed that for the system investigated here, the onset of hydrodynamic instabilities of the laminar bubbly flow model occurs at very low gas flowrates, which are uninteresting from the application standpoint. At values of gas velocities typically used in experimental setups, the flow is in a fully developed turbulent regime. For this reason, we used the steady-state turbulent bubbly flow model to approach the gas–liquid flow in the bubble reactor. In this model, the two phases are assumed to co-exist at any point of the domain (interpenetrating media), the volume fractions occupied by the two phases being $\phi_g(r,z)$, and $\phi_l = 1-\phi_g$ for the gas and the liquid, respectively. The other unknowns solved for in the model are the liquid velocity, $\mathbf{u}_l(r,z)$, the pressure $P(r,z)$ (supposed equal for both phases), the turbulent kinetic energy, $k(r,z)$, and the energy dissipation rate, $\varepsilon(r,z)$. These unknowns are computed from the system of Partial Differential Equations (PDE) enforcing -(i) the momentum balance for the liquid phase, (ii) the continuity of the two-phase mixture, (iii) the (purely convective) transport equation for the volume fraction of the gas, and (iv)-(v) the advection-diffusion transport equations for the turbulent kinetic energy and the dissipation rate (the explicit set of equations and boundary conditions of the model are reported in the Appendix). The model was solved using the commercial software COMSOL Multiphysics. Three different finite element meshes, characterized by 1.8×10^4, 7.5×10^4, and 2.2×10^5 elements, have been tested to investigate mesh convergence. The results of convergence tests are reported in Fig. 12 in Appendix.

In the bubbly flow approach, the relative velocity (henceforth referred to as *slip velocity*, $\mathbf{u}_s = \mathbf{u}_g - \mathbf{u}_l$) of the gas with respect to the liquid is computed through the friction factor C_d by assuming a prescribed bubble size and enforcing the local balance between buoyancy and viscous drag forces. Thus, by definition this velocity is equal to the terminal velocity of a single bubble raising through an infinitely extended molten medium, where $\mathbf{u}_l = 0$. Therefore, the departure of the gas velocity from the terminal velocity value associated with the motion of a single bubble is a *collective effect* of the bubbles, which set the liquid in motion because of their buoyancy, and find themselves entrained in a moving continuum.

2.3. Average gas velocity and average residence time of the bubbles

The solution of the turbulent bubbly flow model provides a detailed knowledge of the local gas velocity, $\mathbf{u}_g(r,z) = \mathbf{u}_s(r,z) + \mathbf{u}_l(r,z)$, as well as of the local turbulent diffusion coefficient, $\mathcal{D}_t(r,z)$, governing the dispersion of individual bubbles about the local streamline of the mean gas flow, and therefore the local volume fraction, ϕ_g of the gas phase. From these variable fields, the average gas velocity of the gas phase is computed as

$$\langle \mathbf{v}_g \rangle = \frac{\int_V (\mathbf{u}_s + \mathbf{u}_l)\,\phi_g \, dV}{\int_V \phi_g \, dV} \tag{2}$$

Finally, the average residence time of the gas is obtained as $\langle t_g \rangle = H / \left| \langle \mathbf{v}_g \rangle \right|$, H being the melt height.

2.4. Conversion of a single methane bubble

As pointed out in the Introduction, in recent articles by some of these authors [29,30], a hierarchy of models with decreasing complexity was developed to evaluate the conversion due to pyrolysis reaction of a single bubble of pure methane entering the reaction melt. In all of these models, it is assumed that temperature and pressure are uniform both in the reaction bath and inside the bubble. We observe that the assumption of constant pressure is well justified both for lab-scale equipment and the industrial scale reactor. In the case of lab-scale reactors, which typically operate at atmospheric pressure, this is because the hydrostatic pressure head is order 10 cm, which corresponds to less than a 10% variation between the top and the bottom of the bath even for high density metals. The same relative variation applies to full scale reactors (even though here the bath height can be order of few meters), since the operating pressure is expected to be 10 atm or larger, depending on the gas distribution grid.

The models developed ranged from the finite element solution on a deformable mesh of the coupled momentum-mass-species transport within the bubble (which is allowed to expand owing to the increasing number of moles in the gas phase) to a completely analytical model explicit in the transport-thermodynamic parameters, which can be written as

$$\frac{X(t)}{X_{\mathrm{eq}}(T,P)} = 1 - \exp\left(-t/t_{\mathrm{srm}}\right); \qquad t_{\mathrm{srm}} = \frac{R}{3\,k_{\mathrm{surf}}(T)} + \frac{R^2}{\pi^2 D(T,P)} \tag{3}$$

Here $k_{\mathrm{surf}}(T)$ is the intrinsic kinetic constant of the (supposedly heterogeneous) reaction occurring at the gas–liquid interface, $\mathcal{D}(T,P)$ is the diffusion coefficient of methane in the gas phase, R is the bubble radius at detachment from the sparger, t_{srm} is the characteristic conversion time, and X_{eq} is the equilibrium conversion at the prevailing temperature and pressure. This latter term allows to account for the effect of equilibrium limitations on the maximum achievable conversion as well as on the rate of the reaction. The analytical model yielded a maximum of 10% discrepancy with respect to the full finite-element solution in the worst case scenario of nearly complete conversion at high temperature, and was tested against available data of methane conversion in NiBi melts lab-scale pyrolysis reactors operating at 1000 °C [7,29], showing an excellent potential for interpreting experiments.

In light of the findings summarized above, here we combine the analytical model developed in [29] and summarized by Eq. (3) with the new two-phase CFD analysis described in the previous paragraphs, which allows to determine the gas average residence time for a reactor of given geometric characteristics and bubble diameter. Such a combination allows the evaluation of methane conversion vs. molten bed height, while accounting for the effect of the presence of a swarm of bubbles on the gas velocity.

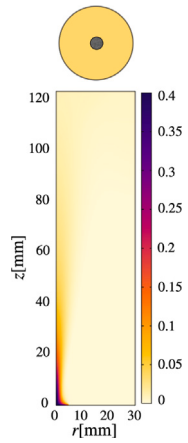

Fig. 2. Gas hold up for a 60 mm diameter reactor, with a 10 mm diameter sparger, fed with a gas flow rate of 50 N mL/min.

3. Results

The results shown below have been obtained by enforcing the turbulent bubbly flow model described in the previous section on an axial-symmetric two-dimensional domain. In this approach, a fundamental piece of information is given by the expression chosen for the drag coefficient, say C_d, of the bubbles (here assumed to be all of the same size when released at the sparger), which fixes the relative slip velocity, $\mathbf{u}_s$, between the gas and the liquid phase. In this regard, a variety of different expressions have been proposed, each taking into account different aspects of bubble dynamics and each appropriate for selected classes of systems (nature of the melt, presence of impurities, fluid-dynamic regimes) [32–34]. Depending on the system at hand, these expressions are not always quantitatively consistent with each other. Yet, they all provide similar values of C_d in the two limiting situations of Stokes flow and Newton's regime, which apply to very small and large bubbles, respectively. To prevent the results next presented from being largely dependent on the model selected for the drag force, we chose to consider only two bubble sizes, namely $d_S = 0.1$ mm and $d_S = 5$ mm, which fall in the two limiting regimes, regardless of the chosen correlation. In all of the cases discussed below, steady-state conditions resulting from a constant flowrate fed at the sparger are enforced. The system of equations defining the bubbly flow model were discretized on an unstructured mesh consisting of order 10^6 degrees of freedom defined on the $r - z$ domain. Given that, to date, most experimental results of methane pyrolysis in molten media have been obtained in lab-scale reactors, we focused on centimeter-scale devices, so that the order of magnitude of the variables solved for can be compared/contrasted with available experimental data. Table 1 summarizes the geometric parameters and operating conditions investigated. The choice of flow rates investigated derives from an analysis of the influence of gas flow rate on hold up. As will be discussed in greater detail in Section 3, an increase in flow rate causes an increase in gas hold up; however, when its value increases above ≈ 20%, neglecting bubble coalescence would be misleading and a different flow model would be required to describe the system. At the same time, such a regime would not be favorable in practical applications, because the contact between liquid and gas would become too low. For this reason, for every set of geometric parameters, the maximum flow rate was chosen so as to avoid an excessive gas hold up. As an example, Fig. 2 shows that, for a 60 mm diameter with a 10 mm sparger, the value of ϕ_g would reach 40% if a gas flow rate of 50 N mL/min were to be employed.

The main physical properties of the two molten media considered are reported in Table 2. All results have been obtained by considering a single value of bubble diameter, equal to 5 mm.

Table 1
Geometric and operating parameters of the systems investigated. Bullets mark the conditions considered for the numerical simulations.

D_m [mm]	30				60			
D_s [mm]	5	10	15	25	10	20	30	50
Q = 10 [N mL/min]	•	•	•	•	•	•	•	•
Q = 20 [N mL/min]	–	•	•	•	•	•	•	•
Q = 50 [N mL/min]	–	–	–	•	–	•	•	•
Q = 100 [N mL/min]	–	–	–	–	–	–	–	•

Table 2
Main physical properties of Gallium and KBr at 1000 °C.

	ρ_l [g/cm^3]	μ_l [m Pa s]	σ [N/m]
Ga	5.5 [35]	0.6 [35]	0.6 [36]
KBr	2 [37]	0.8 [38]	0.07 [37]

3.1. Average residence time and average gas hold-up

We begin our analysis by targeting the average residence time, $\langle t_g \rangle = H / \left| \langle \mathbf{v}_g \rangle \right|$ and the average gas hold-up $\langle \phi_g \rangle = (1/V) \int_V \phi_g \, dV$, which constitute the primary quantities of interest for reactor design. Fig. 3 shows the average residence time of the gas in a 12 cm high melt of KBr at 1000 °C andP = 10 atm, for a reactor diameter $D_m = 30$ mm (panel (a)) and $D_m = 60$ mm (panel (b)), at different values of the sparger-to-reactor diameter ratio and different flowrates. As can be gathered from the data, for both reactor sizes and at all conditions of flowrate and sparger-to-reactor diameter ratio, the residence time is always lower than that of a single bubble of the same diameter rising though an overall static medium, which is represented by the broken line in both panels. For each sparger size, varying the flowrate has little or no effect on the residence time (see Section 3.3 for more details). Also, when the relative size of the sparger is small compared to the reactor diameter, a sizeable reduction of $\langle t_g \rangle$ from the single bubble estimate can be observed. This effect is more pronounced in the 60 mm diameter reactor (with a relative discrepancy of order 300%) than in the slender (30 mm diameter) reactor. In order to investigate the effect of the melt material, we also computed the gas average residence time in the same conditions and for the same operating parameters considered above for molten Gallium, which in the conditions considered shows a higher density (5.5 [35] vs. 2 g/cm^3 [23]) and a considerable higher surface tension (0.6 vs. 0.07 N/m) [36,37]. Fig. 4 reports the simulation results, which show a weaker dependence of the average residence time on the two-phase effect determined by the collective motion of the bubbles. Note that, because of the larger buoyancy force due to the higher density of the melt, the average residence time of the gas is much lower than that associated with molten salts, both under stagnant liquid conditions and when considering the two-phase effect. In the case of large bubbles ($d_b = 5$ mm, not shown for brevity), we found that the effect of two-phase flow on the residence time is altogether negligible in that the discrepancy between the CFD-computed and the single-bubble estimate of this quantity resulted always well below 10%, regardless of the reactor and sparger geometry and of the flowrate. From the analysis of the data discussed above, the first and foremost point to be explained is the virtually negligible effect of flow rate variations on $\langle t_g \rangle$ at constant sparger geometry and bubble size, a behavior observed experimentally in a variety of "cold" (e.g. air–water) bubble reactors and that has been referred to as *homogeneous regime* [39–41] . Fig. 5 shows how the increasing flowrate crossing the reactor causes a proportionally increasing average gas hold-up rather than an increased average gas velocity and thus a reduced value of $\langle t_g \rangle$ (the case show is the same as that of Fig. 3). On a microscopic level, the flowrate-insensitive regime of the residence time is readily explained as soon as one assumes that increasing the feeding pressure upstream the sparger causes an increased detachment frequency of the bubbles

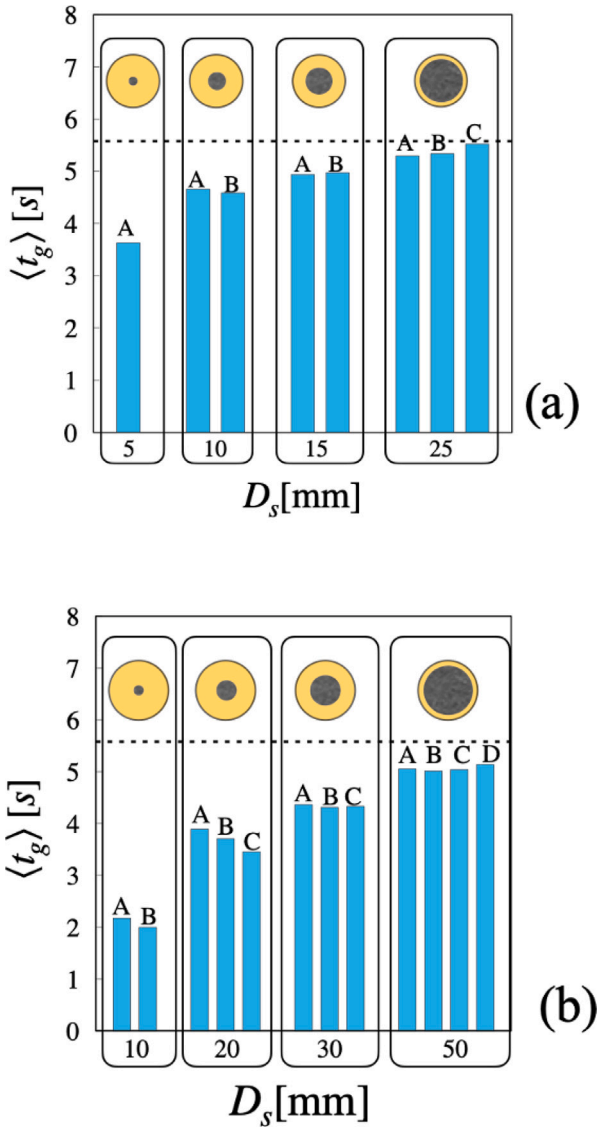

Fig. 3. Average residence time for a 12 cm high melt of KBr at 1000 °C andP = 10 atm for a reactor diameter D_m = 30 mm -(a) and D_m = 60 mm -(b), at different feed flowrates Q, **A** = 10 N mL/min; **B** = 20 N mL/min, **C** = 50 N mL/min **D** = 100 N mL/min. The top images depict the relative size of sparger to the reactor diameter. The bubble size at the sparger is fixed to 0.1 mm. The broken line represents the residence time of a single bubble rising in an overall static melt.

rather than a variation of the bubble size at detachment. In any case, when operating in this regime, one expects that the performance of the pyrolysis reaction (primarily controlled by the gas average residence time) be independent of the flowrate, an occurrence that makes molten reaction environment ideally suited for operating at variable regimes with no loss of efficiency (e.g. in combination with concentrated solar power plants for providing the heat of reaction). The second point to be explained about the $\langle t_g \rangle$ behavior is its sensitive and sizeable dependence on the relative sparger size and on the overall aspect ratio of the melt. As discussed next, understanding the physical mechanism causing this behavior cannot do away with an in-depth analysis of the flow structure of both the liquid and gas phases, as well as of the interplay between the convective a dispersive mechanisms of bubble transport within the melt in defining the local volumetric fraction of the gas phase.

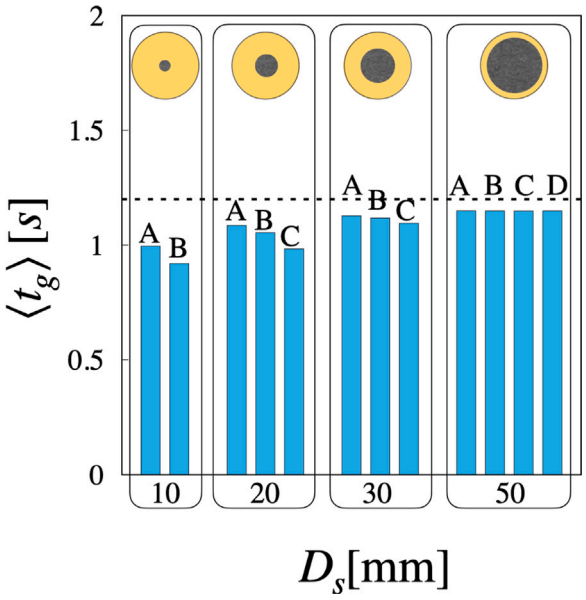

Fig. 4. Average residence time of the gas phase in a Gallium melt at the same conditions as those of Fig. 3 in the 60 mm diameter reactor. The bubble size when released at the sparger is 0.1 mm.

3.2. Two-phase flow

We begin our analysis by focusing on the velocity fields of the liquid and gas phases. Fig. 6 represents the velocity field of the liquid (panels (a) and (c)) and the gas phase (panels (b) and (d)) as a function of the radial (r) and axial (z)coordinates. Panels (a)–(b) and (c)–(d) refer to a sparger-to-reactor diameter ratio D_s/D_m equal to 1/6 and 5/6, respectively. The arrow at the left of each panel provides the scale of the velocity vectors. The bubble size released at the sparger is assumed to be equal to d_b = 0.1 mm. Several observations can be made based on the data depicted. As regards the liquid phase, the flow is purely recirculating, with an uprising velocity located at the axial core of the reactor above the sparger, and descending liquid patterns in proximity of the reactor walls. Note that at any cross-section, the descending velocity of the liquid is less intense than the upward velocity due to the area factor associated with the cylindrical coordinate system (the average liquid flow at any cross-section must add up to zero). For the small sparger the upward-directed liquid flow is significantly different from zero for a large part of the melt height. In the case of the large sparger, the liquid velocity is essentially vanishing in the upper part of the melt. The gas flow is instead everywhere upward oriented and becomes more intense in the axial core region due to the fact that the gas is here entrained in a rising column of liquid, since $\mathbf{v}_g = \mathbf{v}_l + \mathbf{v}_s$, and $\mathbf{v}_l$ and $\mathbf{v}_s$ are oriented in the same direction. The slip velocity is nearly constant (with less than 1% variations), its average value being fixed by the bubble size from the balance of buoyancy and liquid drag. Note that for the bubble diameter here considered, gas and liquid velocities result of the same order of magnitude. When the bubble size is increased to d_b = 5 mm, the resulting structure of the two-phase flow changes remarkably (see Fig. 7). The first difference is quantitative, meaning that the intensity of the liquid velocity is one order of magnitude or even smaller (depending on the sparger size) than that of the gas phase. Also, independently of the sparger size, the rising column of liquid here extends throughout most of the melt height. In any case, as can be gathered from the velocity fields depicted in panels (b) and (d), the effect of the liquid entrainment on the gas velocity is quantitatively irrelevant, especially in the case of the large sparger.

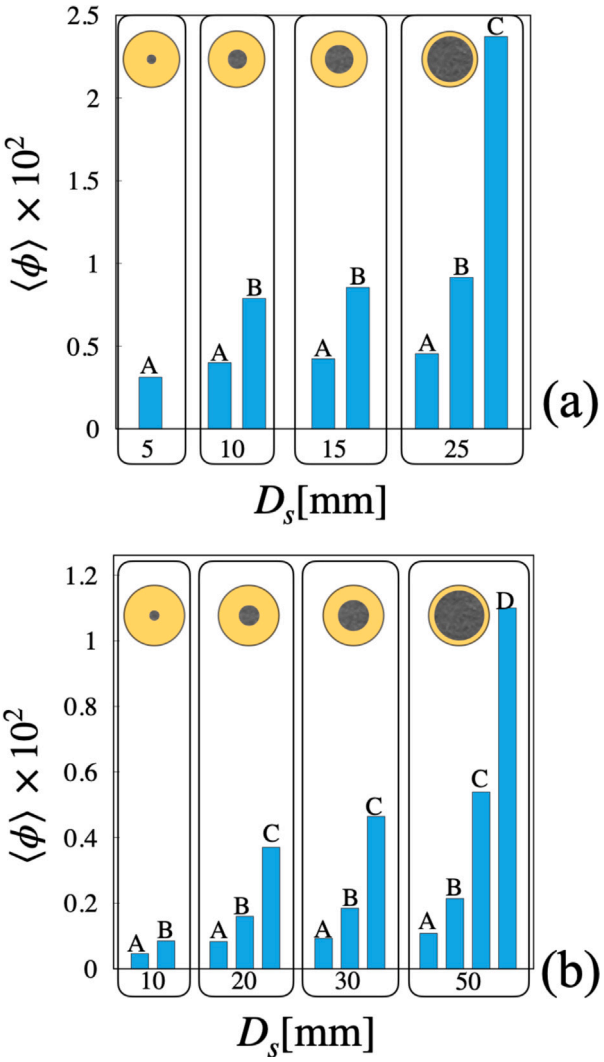

Fig. 5. Average volumetric gas fraction at different values of the relative size of the sparger and increasing gas flowrates. The case shown is the same as that of Fig. 3.i As the flowrate increases from **A** (10 N mL/min) to **B** (20 N mL/min), **C** (50 N mL/min), and **D** (100 N mL/min), the average gas hold-up grows proportionally.

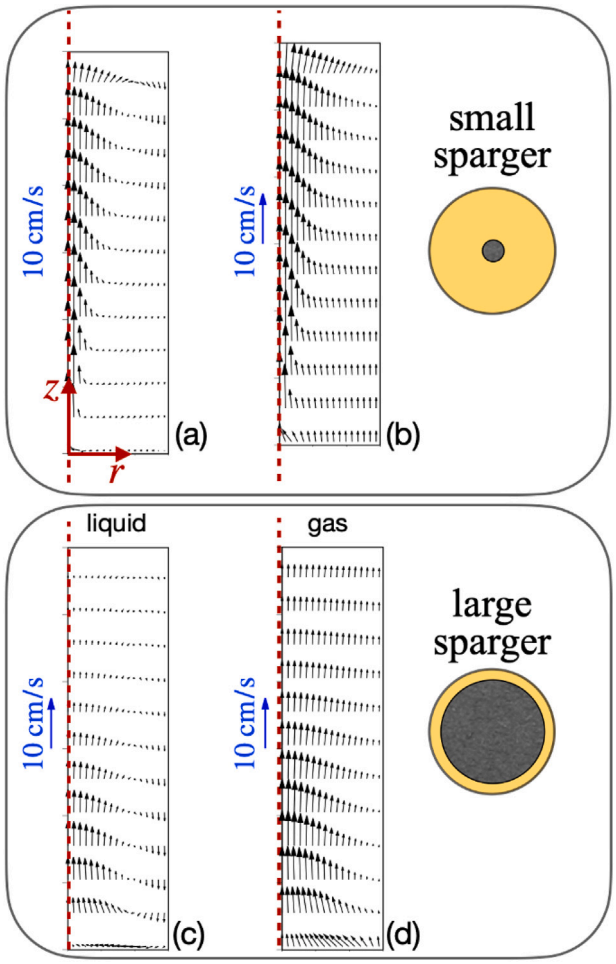

Fig. 6. Flow structure for the liquid and gas phase in a 60 mm diameter cylindrical reactor filled with a 12 cm height melt of KBr at 1000 °C for a bubble size of 0.1 mm. Operating pressure at the top of the melt is fixed at 10 atm. The sparger-to-reactor diameter ratio is equal to 1/6 (panels (a)–(b)) and 5/6 (panels (c)–(d)). Flowrates are fixed to 10 and 50 N mL/min for the small and large sparger, respectively. See main text for details.

3.3. Gas phase distribution

Together with the structure of the gas phase velocity field, an essential piece of information for predicting the average residence time is provided by the local volumetric fraction of the gas phase, ϕ_g, which directly enters as a weighting factor for the average gas velocity defined by Eq. (2). In understanding the relationship between ϕ_g and $\langle \mathbf{v}_g \rangle$, it is useful to expand the right hand side Eq. (2) as the sum of separate contributions from the liquid and slip velocity,

$$\langle \mathbf{v}_g \rangle = \frac{\int_V \mathbf{u}_l \, \phi_g \, dV}{\int_V \phi_g \, dV} + \frac{\int_V \mathbf{u}_s \, \phi_g \, dV}{\int_V \phi_g \, dV} \tag{4}$$

As regards the second term at the right hand side of this relationship, this is almost independent of the structure of the gas volume fraction because the slip velocity $\mathbf{u}_s$ is nearly constant throughout the reactor (order 1% relative variation) and equal to the settling velocity of a single bubble of the given diameter rising through an overall static melt. The value of the first term is instead related to the uniform vs. non-uniform character of the volumetric fraction of the gas phase. To see this, suppose that ϕ_g =constant throughout the entire melt. In this case, the first term at the right hand side of Eq. (4) would simplify to volume average of the liquid velocity, $\langle \mathbf{u}_l \rangle = \int_V \mathbf{u}_l \, dV / \int_V dV$, which must vanish owing to the impermeable boundary conditions enforced for the mass and momentum balance of the liquid phase. Thus in the case of homogeneous spatial distribution of the gas in the entire melt, the average gas velocity equals the average slip velocity, which is primarily controlled by the bubble size through the drag coefficient expression.

Conversely, when ϕ_g displays significant variations, the first term at the right hand side of Eq. (4) may significantly depart from the average liquid velocity. Thus, one expects that deviations of the average gas velocity from the single-bubble uprising settling velocity are tightly connected to the non-uniform distribution of the gas throughout the reaction volume.

To gain insight on the spatial distribution of the gas phase, Fig. 8 shows the local gas fraction ϕ_g (scaled to its average value) for the 6 × 12 cm reactor filled with molten KBr at 1000 °C and P = 10 atm for 0.1 mm bubbles at different values of the sparger-to-reactor diameter ratio. It can be noted how, as the sparger size decreases, larger and larger portions of the melt are devoid of gas (note that the contour scale is logarithmic). The blue continuous lines superimposed to the color map depict an array of selected streamlines of the gas flow spanning uniformly the sparger area. In the case of the small and medium-sized spargers, one notes how the plume of rising gas extends well beyond the convective flux tube defined by the outmost gas streamline

Table 3
Effect of flow rate on liquid velocity and gas hold up for two reactor geometries.

		$\langle \phi_g \rangle = \int_V \phi_g \, dV$	$\mathbf{u}'_g = \int_V \mathbf{u}_l \, \phi_g \, dV$	$\langle \mathbf{u}'_g \rangle = \frac{\int_V \mathbf{u}_l \, \phi_g dV}{\int_V \phi_g \, dV}$
$D_r = 60\ mm$, $D_s = 20\ mm$	$Q = 10$ [NmL/min]	2.83E-7	2.62E-9	0.0093
	$Q = 50$ [NmL/min]	1.26E-6	1.70E-8	0.0135
$D_r = 30\ mm$, $D_s = 25\ mm$	$Q = 10$ [NmL/min]	3.85E-7	4.20E-10	0.0011
	$Q = 50$ [NmL/min]	2.01E-6	2.04E-9	0.0010

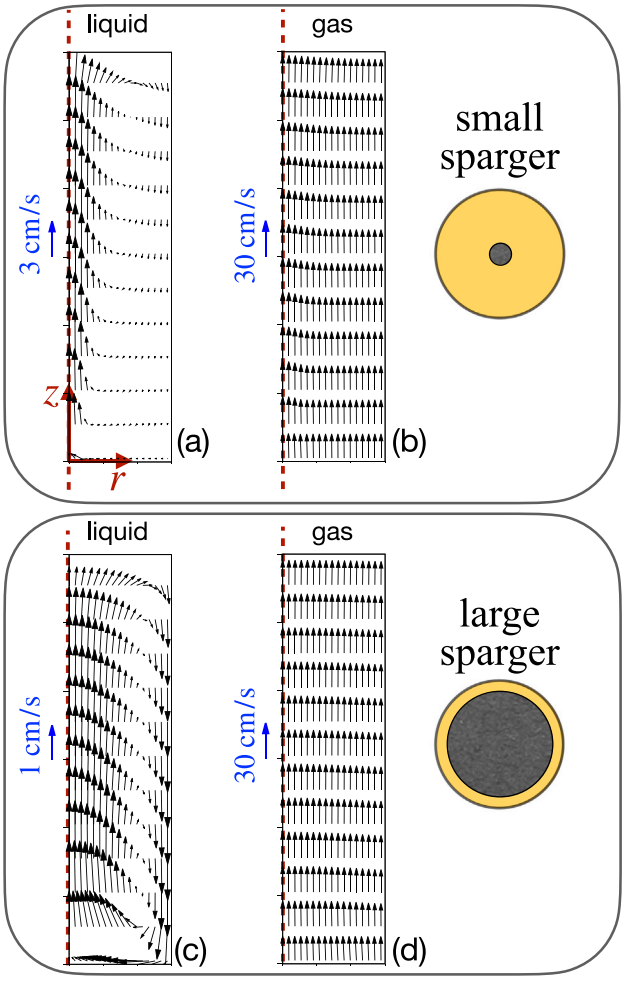

Fig. 7. Flow structure for the liquid and gas phase for a bubble size of 5 mm. Geometric and operating parameters are the same as those of Fig. 6.

departing from the sparger boundary. This suggests that the transport of the gas phase is significantly influenced by the dispersion induced by the turbulent liquid flow (values of the Reynolds number for the case depicted are in the range $4000 \leq \mathrm{Re} \leq 8000$). This is confirmed by the structure of the turbulent dispersion coefficient, D_t, which is reported in Fig. 9 The first observation is that in all cases the typical value of the gas dispersion coefficient is of the same order of magnitude of (or higher than) the diffusion constant of a diluted gas. Also, the field of D_t is strongly non-homogenous in space, with lower values localized at the bottom of the melt. In the case of the larger (5 cm diameter) sparger, the strongest dispersion intensity is observed in the central core of the reaction volume.

The impact of the two phase flow in determining the average residence time reported in the previous section can be mechanistically explained by matching the observations discussed above about the structure of the two-phase flow and those related to the spatial distribution of the gas phase. Fig. 10 reports the side by side comparison of the liquid velocity in panels -(a) and -(c) of Fig. 6 and the gas volume fraction depicted in panels -(a) and -(c) of Fig. 8. In the case of the small sparger, the gas phase is essentially present only in the axial core of the melt. Thus the contribution of the descending (downward directed) liquid near the reactor walls in determining the first integral in Eq. (4) is negligible. As a result, the overall contribution of this integral departs from zero and determines an overall increment of the gas velocity with respect to that of a single bubble rising in a static melt. In the case of the large sparger, the nearly homogeneous gas distributions implies that the first integral is vanishing (as discussed above), so that the average gas velocity and, consequently, the average residence time, $\langle t_g \rangle$, is very close to the single bubble estimate. In this case, the two-phase effect can therefore be neglected.

To further quantify the discussion above, Table 3 reports, for four different operating conditions, the values of the first term on the r.h.s. of Eq. (4), which gives an indication of the departure of the average gas velocity from that of a single bubble in a quiescent liquid, as well as those of its numerator and denominator. A few interesting pieces of information may be gathered from this table. The first observation to be made is that, regardless of reactor geometry, an increase in flow rate causes and increase in the values of both the numerator, u'_g, and denominator, $\langle \phi_g \rangle$. However, the increase in these two terms is not proportional to that of the flow rate. As a result, for the 60 mm reactor, with a 20 mm sparger, an increase in flow rate causes a slight in $\langle u'_g \rangle$, whereas the effect of flow rate is virtually negligible, or even opposite, when the same flow rate conditions are investigated for the 30 mm reactor with 25 mm sparger.

3.4. Impact of two-phase flow effect on overall methane conversion

By enforcing the multiscale approach, the average residence time of the gas computed from the two-phase flow model, can be used to predict the overall methane conversion in the reacting melt through Eq. (3) as

$$\frac{X(t)}{X_{\mathrm{eq}}(T,P)} = 1 - \exp\left(-\langle t_g \rangle / t_{\mathrm{srm}}\right) \tag{5}$$

Fig. 11 shows the comparison between the prediction of the multiscale two-phase approach (bullets) and the estimate obtained for a single bubble rising in a quiescent melt (where $t = H/v_b^{\infty}$ and v_b^{∞} is the terminal rising velocity of the bubble) for a KBr melt at 1030 °C for the 60 mm diameter reactor fed by the small sparger (D_s = 10 mm), for $k_{\mathrm{surf}} = 5 \times 10^{-5}$ m/s and $k_{\mathrm{surf}} = 10^{-5}$ m/s (the order of magnitude of the kinetic constant has been chosen based on the experimental data in similar systems [23]). As can be noted, the relative error between the two estimates can be of order 100%. Depending on the melt height and the value of k_{surf}, the relative error can reach order

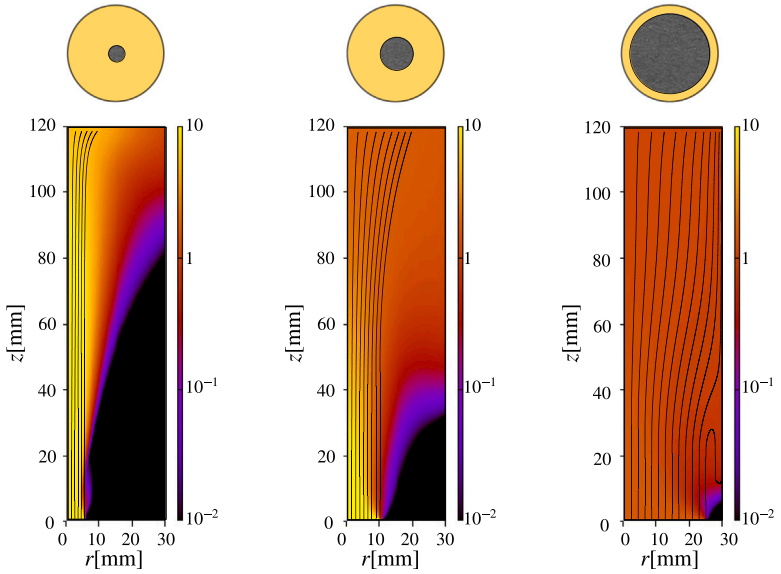

Fig. 8. Volumetric fraction of the gas phase, ϕ_g scaled to its average value for sparger diameters D_s equal to 10,20, and 50 mm and flowrates fixed to 10, 20 and 50 N mL/min going from left to right.

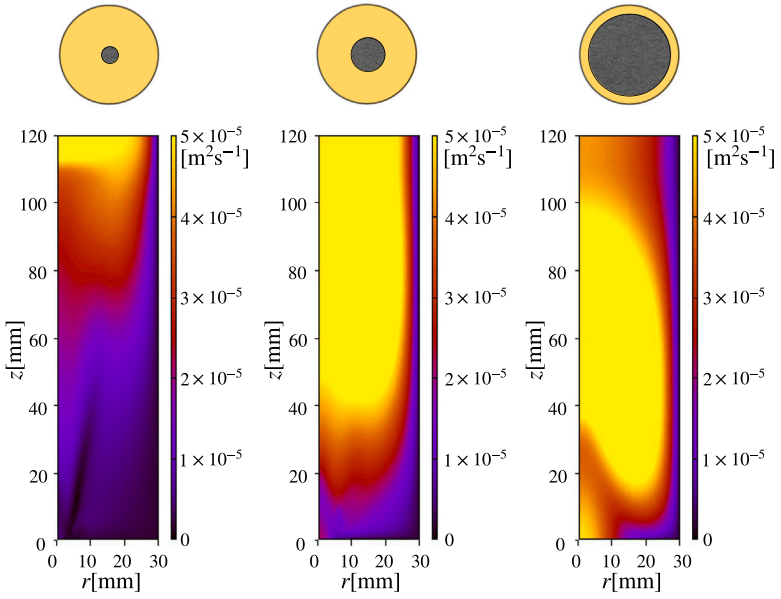

Fig. 9. Intensity of turbulent fluctuations measured through the gas dispersion coefficient, D_t, for the cases shown in Fig. 8.

100%. An important observation can be drawn from the data depicted in Fig. 11 as regards the interpretation of experimental measures of methane pyrolysis lab-scale bubble reactors, whose size falls within the centimeter-scale range considered in this article. Typical experimental campaigns consist of determining the overall methane conversion at different flowrates and compositions of the feed (which may contain inerts). From these measures, the bubble size is estimated from the overall conversion in the melt, by simultaneously solving Eq. (3) under the assumption of kinetics-dominated regime, and $t = H/v_b^\infty$, where the relationship $v_b^\infty = v_b^\infty(d_b)$ is fixed by the model expressing the viscous drag. However, the analysis carried out in this article showed how, due to the liquid lift caused by the bubbles, the effective residence time of the gas can be significantly lower than that predicted by the single-bubble estimate. This implies that the bubble size derived from conversion measurements may be significantly overestimated if the two-phase effect are not taken into proper account.

4. Conclusions and outlook

A multiscale approach to predicting the performance of methane pyrolysis in molten media reactors is presented, where a previously developed analytical model of the conversion within a single methane bubble is combined with the two-phase flow effects driven by the collective buoyancy of the bubbles, which causes a recirculation of the liquid melt. Because the gas is preferentially concentrated in the uprising liquid column, its effective velocity is higher than that of a single bubble of the same size rising through an overall quiescent fluid. This effect is found to increase when the sparger-to-reactor diameter ratio D_S/D_m decreases. Also, the impact of the two-phase flow becomes more evident when the aspect ratio H/D_m of the melt decreases. An in-depth analysis of the underlying mechanisms governing the transport of bubbles reveals that the dependences of $\langle t_g \rangle$ on the D_s/D_m and H/D_m can be pinned down to the widening of the uprising gas plume along

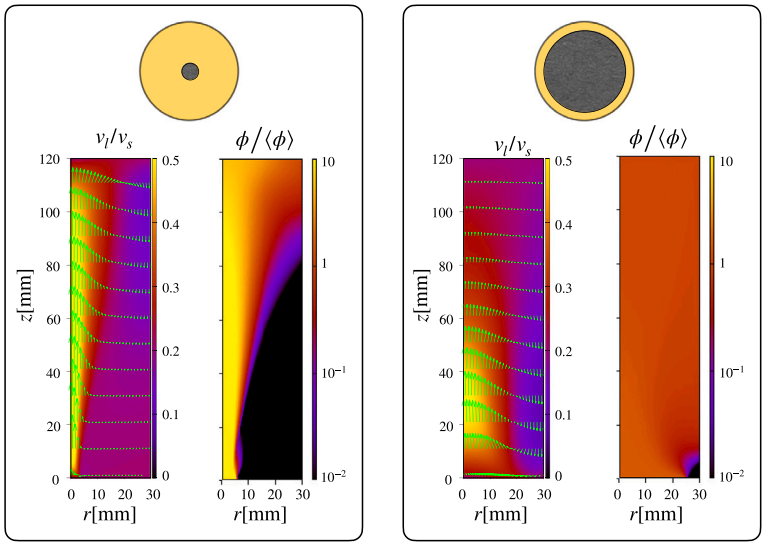

Fig. 10. Side by side comparison of the liquid velocity depicted in panel (a) and (c) of Fig. 6 with the gas volume fraction (left and right panels of Fig. 8). In the case of small sparger, because the gas phase is present only in the axial core of the melt, the contribution of the descending liquid flow near the reactor walls in determining the first integral in Eq. (4) is negligible.

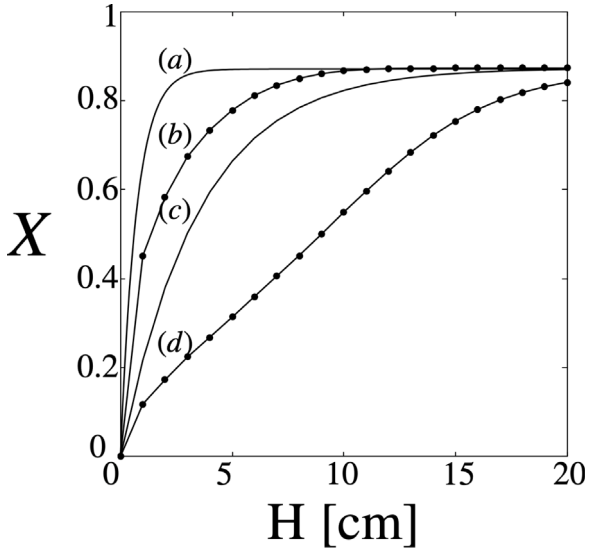

Fig. 11. Comparison between methane conversion as predicted either by the multiscale two-phase approach (bullets) or by assuming a single bubble rising in a quiescent liquid (solid curves) for a KBr melt at 1030 °C andP = 10 atm for values of the surface kinetic constant $k_{surf} = 5 \times 10^{-5}$ m/s (curves (a) and (b)) and $k_{surf} = 10^{-5}$ m/s (curves (c) and (d)).

the axis of the vessel, which is controlled by the streamlines of the gas velocity field and by the dispersion induced by the turbulent motion of the liquid. The results put forward in this article should motivate a re-interpretation of experimental work available in the literature, where the average residence of the gas time is estimated based only on the bubble size, therefore implicitly assuming that the liquid is quiescent. Based on the fact that the two-phase effect always acts in the direction of lowering $\langle t_g \rangle$ with respect to the single bubble in a static fluid, we argue that the estimates of bubble size indirectly derived from the experimental measure of the overall methane conversion may yield a predicted diameter bigger than the actual bubble size. Future work on the multiscale approach proposed should naturally focus on increasing the reactor size to pilot and industrial scales. In this case, the isothermal assumption here enforced for the reaction bath should be carefully considered, as temperature gradients could be expected which cause significant variations of the kinetic constant of the reaction.

CRediT authorship contribution statement

Valentina Biagioni: Writing – original draft, Software, Investigation, Formal analysis. **Giuseppe Procopio:** Writing – original draft, Software. **Antonio Brasiello:** Writing – original draft, Software. **Luca Turchetti:** Writing – original draft, Investigation. **Stefano Cerbelli:** Writing – original draft, Formal analysis, Conceptualization. **Maria Anna Murmura:** Writing – original draft, Investigation.

Declaration of competing interest

The authors declare that they have no known competing financial interests or personal relationships that could have appeared to influence the work reported in this paper.

Acknowledgments

This work was funded by the Italian Ministry of Environment and Energy Security through Ricerca di Sistema Elettrico Nazionale (RdS), the «National Electricity System Research» programme 2022–2024 triennial implementation plan. Integrated project 1.3: Hydrogen Technologies

Appendix. Turbulent bubbly flow model

The model consists of five partial differential equations,

$$\phi_l \rho_l (\mathbf{u}_l \cdot \nabla)\mathbf{u}_l = \nabla \cdot \Big(-p\mathbf{I} + \phi_l(\mu_l + \mu_t)\big(\nabla \mathbf{u}_l + (\nabla \mathbf{u}_l)^T - \frac{2}{3}(\nabla \cdot \mathbf{u}_l)\mathbf{I}\big) - \frac{2}{3}\phi_l \rho_l \, k\mathbf{I} \Big) + \rho_l \phi_l \mathbf{g} \tag{6}$$

$$\nabla \cdot \left(\phi_l \rho_l \mathbf{u}_l + \phi_g \rho_g \mathbf{u}_g\right) = 0 \tag{7}$$

$$\nabla \cdot \left(\phi_g \rho_g \mathbf{u}_g\right) = 0 \tag{8}$$

$$\rho_l (\mathbf{u}_l \cdot \nabla) k = \nabla \cdot \left((\mu_l + \mu_t/\sigma_k)\nabla k \right) + P_k - \rho_l \varepsilon \tag{9}$$

$$\rho_l (\mathbf{u}_l \cdot \nabla) \varepsilon = \nabla \cdot \left((\mu_l + \mu_t/\sigma_\varepsilon)\nabla \varepsilon \right) + C_{1\varepsilon} \frac{\varepsilon}{k} P_k - C_{2\varepsilon} \frac{\varepsilon^2}{k} \tag{10}$$

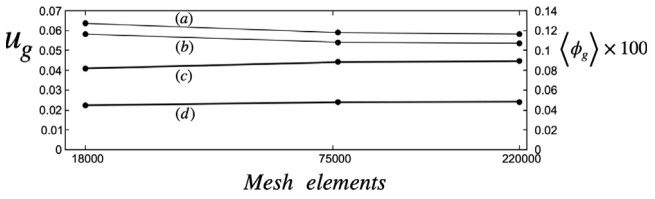

Fig. 12. Average gas velocity (curves a and b) and the average volumetric fraction of the gas phase vs. the number of the mesh elements. Curves (a) and (c) correspond to a flow rate of 10 N mL/min, while curves (b) and (d) correspond to a flow rate of 20 N mL/min.

involving five unknown functions, namely the volumetric fraction of the gas, ϕ (note that $\phi_l = 1 - \phi_g$), the velocity of the liquid phase, $\mathbf{u}_l$, the local pressure, P, (supposed equal for gas and liquid phases) the turbulent kinetic energy, k, and rate of dissipation, ϵ (note that $\phi_l = 1 - \phi_g$) The closure condition determining the uniqueness of the solution is given by the equation of state, $f(P, \rho_g, T)$ describing the volumetric behavior of the gas phase. Given that, even at the industrial scale, the operating pressure is not expected to exceed 20 atm, in what follows the ideal gas law has been assumed to hold true. In the system of Eqs. (6) through (10), $\mu_t = \rho_l C_\mu k^2/\epsilon$, and P_k is defined as

$$P_k = \mu_t \left(\nabla \mathbf{u}_l : \left(\nabla \mathbf{u}_l + (\nabla \mathbf{u}_l)^T \right) - \frac{2}{3} \left(\nabla \cdot \mathbf{u}_l \right)^2 \right) - \frac{2}{3} \rho_l k \nabla \cdot \mathbf{u}_l \tag{11}$$

The local balance equations above are equipped with the boundary conditions,

$$\begin{aligned} &\mathbf{u}_l \cdot \mathbf{n} = 0; \quad \mathbf{K_n} - \left(\mathbf{K}_n \cdot \mathbf{n} \right) \mathbf{n} = 0 \qquad \nabla k \cdot \mathbf{n} = 0; \\ &\nabla \epsilon \cdot \mathbf{n} = 0; \quad -\mathbf{n} \cdot \mathbf{N}_g = N_g^{\text{in}} \end{aligned} \tag{12}$$

at the sparger surface (here $\mathbf{K}_n = \mathbb{K} \cdot \mathbf{n}$, $\mathbb{K}$ being the viscous stress tensor), $\mathbf{N}_g$ is the local mass flowrate of the gas phase,

$$\begin{aligned} &\mathbf{u}_l \cdot \mathbf{n} = 0; \quad \mathbf{K_n} = \rho_l \frac{u_\tau}{u^+} \left(\mathbf{u}_l - (\mathbf{u}_l \cdot \mathbf{n}) \mathbf{n} \right) \quad ; \\ &\nabla k \cdot \mathbf{n} = 0; \quad \epsilon = \frac{\rho_l C_\mu k^2}{\kappa_v \delta_w^+ \mu_l} \quad -\mathbf{n} \cdot \mathbf{N}_g = 0 \end{aligned} \tag{13}$$

$$\mathbf{u}_l \cdot \mathbf{n} = 0; \quad \mathbf{K_n} - \left(\mathbf{K}_n \cdot \mathbf{n} \right) \mathbf{n} = 0 \quad \nabla k \cdot \mathbf{n} = 0; \quad \nabla \epsilon \cdot \mathbf{n} = 0 \tag{14}$$

at the gas–liquid interface at the top of the molten bath.

The slip velocity of the bubbles can be obtained from the momentum equation for the gas phase:

$$\nabla p = \mathbf{f_d} \quad \mathbf{f_d} = -C_d \frac{3}{4} \frac{\rho_l}{d_b} |u_{slip}| u_{slip} \tag{15}$$

The drag coefficient (C_d) related to the bubbles characterized by a diameter equal to 100 μm has been derived from the Hadamard–Rybczynski model [42]:

$$C_d = \frac{16}{Re_b}, \tag{16}$$

$$Re_b = \frac{d_b \rho_l |u_s|}{\mu_l} \tag{17}$$

where d_b is the bubble diameter, u_s is the slip velocity of the bubbles, and μ_l and ρ_l are the viscosity and density of the medium, respectively .

For the bubbles with a diameter of 5 mm, the drag coefficient (C_d) has been estimated as follows [31] :

$$C_d = \frac{0.622}{\frac{1}{E\ddot{o}} + 0.235}, \tag{18}$$

$$E\ddot{o} = \frac{g \rho_l d_b^2}{\sigma} \tag{19}$$

where σ is the surface tension coefficient of the medium, and g is the standard gravity .

Results of convergence tests are reported in Fig. 11.

References

[1] Alhamed H, Behar O, Saxena S, Angikath F, Nagaraja S, Yousry A, Das R, Altmann T, Dally B, Sarathy SM. From methane to hydrogen: A comprehensive review to assess the efficiency and potential of turquoise hydrogen technologies. Int J Hydrog Energy 2024;68:635–62.

[2] Msheik M, Rodat S, Abanades S. Methane cracking for hydrogen production: A review of catalytic and molten media pyrolysis. Energies 2021;14(11):3107.

[3] Guo L, Tan J, Ren J, Guo Z. Methane catalytic cracking by solid materials and molten media for hydrogen production: A review. J Renew Sustain Energy 2024;16(2).

[4] Weger L, Abánades A, Butler T. Methane cracking as a bridge technology to the hydrogen economy. Int J Hydrog Energy 2017;42(1):720–31.

[5] Korányi TI, Németh M, Beck A, Horváth A. Recent advances in methane pyrolysis: turquoise hydrogen with solid carbon production. Energies 2022;15(17):6342.

[6] Guéret C, Daroux M, Billaud F. Methane pyrolysis: thermodynamics. Chem Eng Sci 1997;52(5):815–27.

[7] Upham DC, Agarwal V, Khechfe A, Snodgrass ZR, Gordon MJ, Metiu H, McFarland EW. Catalytic molten metals for the direct conversion of methane to hydrogen and separable carbon. Science 2017;358(6365):917–21.

[8] Abbas HF, Daud WW. Hydrogen production by methane decomposition: a review. Int J Hydrog Energy 2010;35(3):1160–90.

[9] Bayat N, Rezaei M, Meshkani F. Methane decomposition over Ni–Fe/Al2O3 catalysts for production of COx-free hydrogen and carbon nanofiber. Int J Hydrog Energy 2016;41(3):1574–84.

[10] Qian JX, Chen TW, Enakonda LR, Liu DB, Mignani G, Basset J-M, Zhou L. Methane decomposition to produce COx-free hydrogen and nano-carbon over metal catalysts: A review. Int J Hydrog Energy 2020;45(15):7981–8001.

[11] Ashik U, Daud WW, Abbas HF. Production of greenhouse gas free hydrogen by thermocatalytic decomposition of methane–A review. Renew Sustain Energy Rev 2015;44:221–56.

[12] Schultz I, Agar DW. Decarbonisation of fossil energy via methane pyrolysis using two reactor concepts: Fluid wall flow reactor and molten metal capillary reactor. Int J Hydrog Energy 2015;40(35):11422–7.

[13] Parolin G, Borgogna A, Iaquaniello G, Salladini A, Cerbelli S. Deactivation-induced dynamics of the reaction front in a fixed-bed catalytic membrane reactor: Methane cracking as a case study. Int J Hydrog Energy 2021;46(38):20159–70.

[14] Amin A, Epling W, Croiset E. Reaction and deactivation rates of methane catalytic cracking over nickel. Ind Eng Chem Res 2011;50(22):12460–70.

[15] Hamdan M, Halawy L, Aramouni NAK, Ahmad MN, Zeaiter J. Analytical review of the catalytic cracking of methane. Fuel 2022;324:124455.

[16] Zhang T. Recent advances in heterogeneous catalysis for the nonoxidative conversion of methane. Chem Sci 2021;12(38):12529–45.

[17] Tyrer D. Production of hydrogen. 1931, p. 28, USA Patent 1803221.

[18] Pérez BJL, Jiménez JAM, Bhardwaj R, Goetheer E, van Sint Annaland M, Gallucci F. Methane pyrolysis in a molten gallium bubble column reactor for sustainable hydrogen production: Proof of concept & techno-economic assessment. Int J Hydrog Energy 2021;46(7):4917–35.

[19] Paxman D, Trottier S, Nikoo M, Secanell M, Ordorica-Garcia G. Initial experimental and theoretical investigation of solar molten media methane cracking for hydrogen production. Energy Procedia 2014;49:2027–36.

[20] Zaghloul N, Kodama S, Sekiguchi H. Hydrogen production by methane pyrolysis in a molten-metal bubble column. Chem Eng Technol 2021;44(11):1986–93.

[21] Parkinson B, Patzschke C, Nikolis D, Raman S. Molten salt bubble columns for low-carbon hydrogen form CH_4 pyrolysis: mass transfer and carbon formation mechanisms. Chem Eng J 2021;417:127407.

[22] Kang D, Rahimi N, Gordon MJ, Metiu H, McFarland EW. Catalytic methane pyrolysis in molten MnCl2-KCl. Appl Catal B 2019;254:659–66.

[23] Palmer C, Tarazkar M, Gordon M, Metiu H, McFarland E. Methane pyrolysis in low-cost, alkali-halide molten salts at high temperatures. Sustain Energy Fuels 2021;5:6107–23.

[24] Mouza A, Dalakoglou G, Paras S. Effect of liquid properties on the performance of bubble column reactors with fine pore spargers. Chem Eng Sci 2005;60(5):1465–75.

[25] Kim J, Oh C, Oh H, Lee Y, Seo H, Kim YK. Catalytic methane pyrolysis for simultaneous production of hydrogen and graphitic carbon using a ceramic sparger in a molten NiSn alloy. Carbon 2023;207:1–12.

[26] Anastasiou A, Kazakis N, Mouza A, Paras S. Effect of organic surfactant additives on gas holdup in the pseudo-homogeneous regime in bubble columns equipped with fine pore sparger. Chem Eng Sci 2010;65(22):5872–80.

[27] Wang T, Wang J, Jin Y. Population balance model for gas- liquid flows: Influence of bubble coalescence and breakup models. Ind Eng Chem Res 2005;44(19):7540–9.

[28] Nagashima A. Viscosity, thermal conductivity, and surface tension of high-temperature melts. Int J Thermophys 1990;11:417–32.

[29] Sperelli F, Biagioni V, Gabriele A, Murmura MA, Cerbelli S. Analytic prediction of the effective reaction rate for methane cracking in molten catalysts: Transition from kinetics-dominated to diffusion-limited regimes. Int J Hydrog Energy 2024;53:554–61.

[30] Borgogna A, Iaquaniello G, Biagioni V, Murmura MA, Annesini MC, Cerbelli S, et al. Estimate of the height of molten metal reactors for methane cracking. Chem Eng Trans 2022;96:427–32.
[31] Sokolichin A, Eigenberger G, Lapin A. Simulation of buoyancy driven bubbly flow: established simplifications and open questions. AIChE J 2004;50(1):24–45.
[32] Tomiyama A. Struggle with computational bubble dynamics. Multiph Sci Technol 1998;10(4):369–405.
[33] Chen Y, Wang L, Chang H, Zhang Q. A review of drag coefficient models in gas-liquid two-phase flow. ChemBioEng Rev 2023;10(3):311–25.
[34] Kelbaliyev G, Ceylan K. Development of new empirical equations for estimation of drag coefficient, shape deformation, and rising velocity of gas bubbles or liquid drops. Chem Eng Commun 2007;194(12):1623–37.
[35] Spells K. The determination of the viscosity of liquid gallium over an extended nrange of temperature. Proc Phys Soc 1936;48(2):299.
[36] Alchagirov B, Mozgovoi A. The surface tension of molten gallium at high temperatures. High Temp 2005;43(5).
[37] Janz G. Molten salts handbook. Elsevier Science; 2013, URL https://books.google.it/books?id=K9jXCwMCZeQC.
[38] Belikov V. Pharmaceutical chemistry: textbook. 2nd ed.. MED Press Inform, M.; 2008.
[39] Monahan SM, Vitankar VS, Fox RO. CFD predictions for flow-regime transitions in bubble columns. AIChE J 2005;51(7):1897–923.
[40] Yang JH, Yang J-I, Kim H-J, Chun DH, Lee H-T, Jung H. Two regime transitions to pseudo-homogeneous and heterogeneous bubble flow for various liquid viscosities. Chem Eng Process: Process Intensif 2010;49(10):1044–50.
[41] Kazakis N, Papadopoulos I, Mouza A. Bubble columns with fine pore sparger operating in the pseudo-homogeneous regime: Gas hold up prediction and a criterion for the transition to the heterogeneous regime. Chem Eng Sci 2007;62(12):3092–103.
[42] Crowe C, Schwarzkopf J, Sommerfeld M, Tsuji Y. Multiphase flows with droplets and particles. Taylor & Francis; 1997, URL https://books.google.it/books?id=CioXotlGMiYC.